This is a preproof accepted article for *Clay Minerals*
This version may be subject to change during the production process
DOI: 10.1180/clm.2025.10014

Implications of illite XRD characteristics and K-Ar dating for the tectonics of Mallorca (Spain)

J. Środoń[1*], M. Szczerba[1] and M. Bojanowski[2]

[1] *Institute of Geological Sciences, Polish Academy of Sciences, Senacka 1, 31-002 Krakow, Poland*

[2] *Institute of Geological Sciences, Polish Academy of Sciences, Twarda 51/55, Warsaw, Poland*

Running head: *Implications of illite XRD and K-Ar for the tectonics of Mallorca*

DOI:

Submitted: 29 April 2025. Revised: 27 August 2025. Associate Editor: Martine Buatier

*E-mail: ndsrodon@cyf-kr.edu.pl

ABSTRACT: Serra de Tramuntana of Mallorca is a mountain range built of a stack of thrust sheets, composed mostly of Mesozoic platform carbonates, and formed in the Oligocene and Miocene during the Alpine orogeny. Volcanic rocks, intruding the Triassic sediments, and known mostly from the bottom of the lowest thrust sheet, offer an opportunity of dating the post-sedimentary thermal history and evaluating the maximum paleotemperatures by studying mineralogy and K-Ar dating of authigenic illite. Such study was conducted on sixteen samples from two outcrops, employing X-ray diffraction, optical microscopy, electron probe microanalysis, and K-Ar dating of separated clay fractions. Illite was found in ten samples, but only one sample was identified as pure volcanic rock, not contaminated by older detrital

material. This sample yielded the K-Ar age of 133-140 Ma, the same within the experimental error for three grain-size fractions, confirmed by extrapolating ages of a contaminated sample, and interpreted as representing the age of the maximum paleotemperatures. These paleotemperatures were estimated using several illite characteristics, including the Kubler index applied to shales, as below but close to the diagenesis/anchimetamorphism boundary (180-200^{o}C). The dated pre-tectonic early Cretaceous thermal event is interpreted as recording the extremely high geothermal gradient at the end of the Mesozoic extensional phase. The maximum paleotemperatures during the Oligocene-Miocene tectonic burial of Mallorca were not high enough to reset the Mesozoic K-Ar age of illite, thus lower than c. 250 ^{o}C, and, based on the preserved Cretaceous illite XRD characteristics, lower than 180-200 ^{o}C.

Keywords: Balearic Promontory, Cenozoic thrusting, diagenesis, geothermal gradient, Mesozoic extension, Serra de Tramuntana, shallow burial illitization.

INTRODUCTION

Illite-smectite and illite is a unique clay mineral group which undergoes gradual evolution in the course of diagenesis, and then anchi- and epimetamorphism. This evolution can be quantified, which allows evaluating the grade of diagenesis/metamorphism, but also it can be dated by the K-Ar and Ar-Ar methods, using the potassium content of illite and the resistance of illite to alteration in the course of uplift and weathering. Moreover, this mineral group is very common on the Earth's surface, accounting for 15-30 % of the mass of sedimentary rocks (Garrels & Mackenzie, 1971; War, 2022, discussion in Środoń, 2025). These characteristics make illite-smectite and illite minerals a powerful tool for studying diagenetic and metamorphic

https://doi.org/10.1180/clm.2025.10014 Published online by Cambridge University Press

processes in c. 70-350^{o}C temperature range, and the tectonic histories of orogens (e.g. Hoffman and Hower, 1979; Hunziker *et al*., 1986; Środoń, 2007).

Below the closing temperature of illite (c. 250^{o}C; Hunziker *et al*., 1986), the K-Ar and Ar-Ar methods date the period of maximum paleotemperatures (fast burial) or, in case of a very slow burial, also the earlier period, after c. 70^{o}C paleotemperatures were reached, if several submicron size fractions are dated (Środoń *et al*., 2002). At these low temperatures, contamination by detrital (recycled) illite is the major analytical problem, and has to be avoided as much as possible. At higher metamorphic grades, the period of cooling to the illite closing temperature is dated. In such situation, the detrital illite does not pose a problem, as it also becomes isotopically reset, but potassium minerals with higher closing temperatures (micas) have to be avoided.

In this contribution, illite was used to evaluate the degree and timing of diagenetic/metamorphic alteration of sedimentary rocks building the Serra de Tramuntana mountain range of Mallorca. The majority of Tramuntana rocks are carbonates, but authigenic illites were found in the course of this study in the siliciclastic rocks, including volcanics, known from the Buntsandstein and Keuper series (Navidad & Alvaro, 1985; Enrique, 1986, 2012, 2016; Fornos & Gelabert, 1995). To the knowledge of the present authors, such studies have not been conducted so far in Serra de Tramuntana. Mallorca is considered most often as the north-eastern termination of the Betic Cordillera but this tectonic position has been disputed (Bourrouilh, 2016). It was hoped that studying Mallorca diagenesis/metamorphism may help solving this controversy.

https://doi.org/10.1180/clm.2025.10014 Published online by Cambridge University Press

STUDY AREA

Mallorca, the largest of Balearic Islands, i.e. of the emerged part of the Balearic Promontory, consists of three parallel mountain ranges trending NE-SW, and the Tertiary basins between them. The Balearic Promontory is interpreted as the offshore prolongation of the Betic Cordillera in Spain and is surrounded by the Valencia Trough to the northwest, the Algerian Basin to the south, and the Liguro-Provençal Basin to the northeast. The geological structure of Mallorca is interpreted as the result of three stage evolution: 1) an extensional Mesozoic pre-orogenic stage; 2) a contractional Oligo–Miocene orogenic stage and 3) a Late Miocene to Recent post-orogenic stage (Sàbat *et al*., 2011).

Serra de Tramuntana is located in the northwestern part of Mallorca. Like the entire Betic thrust and fold belt, it was formed during the Alpine orogeny, from the Oligocene, when the thrusting from SE to NW of undeformed sedimentary column had started, to the Late Miocene, when the present-day tectonic structure was formed (cf. Fig. 18 in Sàbat *et al*., 2011). The mountains are composed of a series of thrust sheets involving post-Variscan sedimentary column, starting from Permian red shales and conglomerates (Fig. 1). Triassic is represented by typical Germanic facies: red sandstones and mudstones (Buntsandstein), dolomites and limestones (Muschelkalk), and marls plus evaporates (Keuper). Late Triassic and Jurassic rocks are platform limestones and dolomites, which dominate the mountain ridges of Serra de Tramuntana. Lower Cretaceous rocks are marls and limestones, representing a deeper sea environment. The total thickness of the Mesozoic sedimentary column reaches 1600 m (Fig. 1). A stratigraphic gap (c. 30 Ma) follows, embracing Late Cretaceous and Early Eocene. Sedimentation resumed in Middle Eocene as freshwater limestones, followed by alluvial conglomerates, marine sandstones, and turbidites, interpreted as synorogenic deposits. Post-

https://doi.org/10.1180/clm.2025.10014 Published online by Cambridge University Press

orogenic, flat-lying Late Miocene and Pliocene shallow marine carbonates complete the sedimentary column (Ramos-Guerrero *et al*., 1989; Sàbat *et al*., 2011). The total thickness of the Cenozoic sedimentary column reaches 1300 m (Fig. 1).

The volcanic rocks, potentially suitable for the present study (possible content of authigenic illite non-contaminated by detrital illite) are known from two Triassic formations: Buntsandstein and Keuper, thus ranging in age from the Early Triassic (<250 Ma) to Late Triassic, Norian (>210 Ma). The volcanics are picritic and olivine submarine basalts and teschenite flows, sills, dikes, volcaniclastics, and pyroclastics, highly spilitized, that were emplaced in an intracontinental extensional regime (Navidad & Alvaro, 1985; Enrique, 1986, 2012, 2016; Fornos & Gelabert, 1995). Chlorite, albite, serpentine, iron oxides and hydroxides, calcite, chalcedony, and illite were observed as the alteration minerals, in the outcrops located exclusively in Serra de Tramuntana, mostly at the seashore (Enrique, 1986, 2016).

MATERIALS AND METHODS

Enrique (1986) presented detailed descriptions and maps of five locations with outcrops of the Triassic volcanic rocks. For the purpose of this study, two locations: Port de Valldemossa and Cala Tuent were selected as most promising because of the highest degree of alteration observed by Enrique (1986), including the illitic alteration in Port de Valldemossa. 6 samples, identified macroscopically as volcanics and two as red shales were collected in Port de Valldemossa, both SW and NE of the port (Table 1, Fig. 2a). In Cala Tuent, 3 volcanic samples and one red shale were collected from the vertical outcrop by the road, and two volcanic samples on each side of the beach (Table 1, Fig. 2b). Figure 3 presents photos of most sample locations.

https://doi.org/10.1180/clm.2025.10014 Published online by Cambridge University Press

All the collected samples were studied by X-ray diffraction as bulk rocks in order to check the presence and quantity of illite. Four samples regarded as containing abundant volcanic components and with the highest content of illite were separated into >2, 2-0.5, 0.5-0.2, <0.2 μm fractions, using Jackson (1975) procedure (details in Środoń & Jewuła, 2025), in order to characterize illite in detail. As the amounts of <0.2 μm fractions were not sufficient, oriented preparations of 0.2-0.5 μm fractions were X-rayed both in the air-dry and the glycolated state. All fractions were X-rayed also as random powders, in order to identify and quantify polytypes. The quantitative mineralogical analyses were carried out using the Profex/BGMN software, utilizing Rietveld refinement. During refinement, muscovite $2M_1$, illite 1M, and illite-smectite $1M_d$ were optimized including preferred orientation to achieve the best correspondence between experimental and calculated diffractograms. In the models of muscovite $2M_1$ and illite 1M, anisotropic broadening of reflections was considered, with separately optimized parameters for 00l, and hkl reflections. The structure of illite-smectite $1M_d$ was taken from Ufer *et al*. (2012), in which hkl and 00l reflections were calculated separately. The structure for 00l reflections assumed R1 mixed layered ordering with percentage of illite above 90%, and swelling interlayers containing 2 and 1 layers of water. Higher Reichweite values were not considered due to very good quality of fit achieved with the R1 model.

Additionally, <2 μm fractions were separated from three shale samples and the clay sample CT-4 using Jackson (1975) procedure and final Ca-exchange, in order to measure the full width at half maximum of the 001 illite reflection (FWHM), recorded using the following conditions: incident slit 0.5 ^{o}, receiving slit 10 mm, scanning rate 0.3 ^{o}/min. FWHM was standardized into the Kubler index (KI) following Warr & Ferreiro-Mählmann (2015) by means

https://doi.org/10.1180/clm.2025.10014 Published online by Cambridge University Press

of the experimental regression based on Warr (2018) standards, used in the clay laboratory of the Institute of Geological Sciences PAS in Krakow:

KI = 1.167*FWHM- 0.057

The separated clay fractions of four samples were dated using the K-Ar technique of the clay laboratory of the Institute of Geological Sciences PAS in Krakow (details of the technique in Środoń *et al*. 2023). These four samples were also observed in polished thin sections under a Nikon Eclipse LV100POL polarizing microscope to aid the interpretation of the XRD and K-Ar data. The illite age analysis was conducted for sample PdV-1, with uncertainties in the extrapolated ages estimated using the Monte Carlo method (10000 iterations), taking into account the 2σ confidence intervals for the age and the percentage of detrital potassium. Illites in one sample (PdV-7) were analysed chemically using a Cameca SX-100 electron probe microanalyzer (EPMA) equipped with wavelength-dispersive X-ray spectrometers (WDS) at the Faculty of Geology, University of Warsaw. The sample (polished thin section) was coated with a 20 nm carbon layer prior to analysis. The acceleration voltage was 15 kV, beam current was 8 nA, and the beam diameter was 3 μm. The following diffracting crystals and X-ray lines (in brackets) were used: PC0 (F K_α, and Na K_α), TAP (Mg K_α, Si K_α, and Al K_α), LPET (K K_α, Ca K_α, Cl L_α and Ba K_α), and LIF (Fe K_α, Mn K_α, V L_α and Ti L_α,). The following standard substances were used: albite for Na, MgO for Mg, diopside for Si and Ca, $BaSO_4$ for Ba, Fe_2O_3 for Fe, rhodonite for Mn, orthoclase for Al and K, V_2O_5 for V, topaz-F for F, tungupite for Cl, $LaPO_4$ for P, and TiO_2 for Ti.

https://doi.org/10.1180/clm.2025.10014 Published online by Cambridge University Press

RESULTS

Bulk rock XRD data

The characteristic XRD patterns of the Cala Tuent bulk rock samples are shown in Fig. 4. Most samples represent the compositional range between CT-5 (relatively fresh basalt rock rich in plagioclase and pyroxene, with some quartz, orthoclase, hematite, calcite, and chlorite, sometimes mixed-layered) and CT-3 (strongly altered basalt with plenty of chlorite and hematite, some anatase, orthoclase, calcite, quartz, plagioclase, and traces of illite). Two samples: red shale CT-8 and soft clay CT-4 are different (Fig. 4). They also contain chlorite, orthoclase, carbonates, hematite in the red shale, but no plagioclase, the percent of quartz is much higher, and there is plenty of illite. The CT-4 sample was selected for K-Ar dating and more detailed mineralogical study.

Most of the Port de Vallemossa samples of the rocks, identified macroscopically as hard volcanic intrusions, have mineral composition ranging from PdV-4 to PdV-6 (Fig. 5) and typically contain abundant quartz and $2M_1$ illite/mica, along with variable amounts of dolomite and calcite, small amounts of 1M illite, anatase, and rutile, and trace amount of dawsonite. Red shale samples have similar mineral composition and an additional abundance of hematite (PdV-3 shown in Fig. 5). The hard yellow PdV-7 rock (Fig. 3C), also identified macroscopically as volcanic tuff/intrusion has a very different composition, indicative of volcanic origin with less quartz, abundant mixed-layer 1M illite, tridimite-2OH and dolomite, along with small amounts of barite, anatase, and probably sphalerite (Fig. 5). PdV-1, PdV-6, and PdV-7 samples were selected for K-Ar dating and more detail mineralogical study.

https://doi.org/10.1180/clm.2025.10014 Published online by Cambridge University Press

Clay fraction XRD data

Representative XRD patterns of oriented 0.5-0.2 μm fractions, both air-dry and glycolated, are presented in Fig. 6. Illites in all samples display characteristic indications of traces of swelling: 001 reflection after glycolation is narrower and displaced towards higher angles, while 002 and 003 reflections towards lower angles (if swelling is sufficiently strong: in PdV-7). Intensity ratio of 001/003 reflections decreases after glycolation, producing Ir index >1 (Ir= [001/002 air]/[001/003gly] = 1.0 for non-swelling illite; Środoń, 1984). 005 reflection is not split, which is indicative of the percent of swelling layers below 10 (Środoń *et al*., 2009), highest in PdV-7 (Ir=1.46). d_{005} of 1.999 Å indicates potassium illite without detectable Na or NH_4 substitutions. The patterns of PdV-6 (not shown in Fig. 6) are very similar to PdV-1. The Kubler index measurements on <2 μm fractions gave diagenetic values from 0.70 to 1.03 $^{o}2\theta$ CuK_{α}, and are reported in Table 1.

All random patterns of clay-size fractions display characteristic variation with respect to grain size (Table 2, Fig. 7): in coarser fractions there is more $2M_1$ illite and quartz, and illite reflections are narrower. All samples except PdV-7 contain mixtures of $2M_1$ and 1M illite polytype. Both $1M_{tv}$ and $1M_{cv}$ varieties are detectable. $1M/2M_1$ ratio decreases in coarser fractions, which is evident from the relative peak intensities and was confirmed by the polytype quantification (Table 2; Fig. 8). In PdV samples, d_{060} is close to 1.500 A (Table 3), indicative of aluminous composition. In the CT-4 sample, the 060 reflection of illite overlaps with a strong chlorite reflection. In PdV-7, only the 1M illite polytype is present. $1M_{tv}$ is dominant but $1M_{cv}$ can also be detected. The 001 region of PdV-7 demonstrates that illite in this sample is composed of a coarse, non-expandable variety, dominating in 2-0.5 μm fraction, and an expandable variety, abundant in <0.2 μm fraction.

https://doi.org/10.1180/clm.2025.10014 Published online by Cambridge University Press

Petrographic observations

The four samples selected for K-Ar dating were also investigated using a polarizing microscope. The detrital material was not observed only in one of them (PdV-7), which is a highly altered rock composed mostly of fine-crystalline illite (Fig. 9A, B). The rock fabric, although obliterated by this secondary illite to some extent, resembles a diabasic texture suggesting a (sub)volcanic origin. This sample was also analyzed using the EPM, which enabled mineral identification of some components. Illite occurs as pseudomorphs probably replacing lath-shaped feldspars and platy biotite, and as matrix between these pseudomorphs. A TiO_2 mineral (anatase according to XRD; Fig. 5) was detected in the rock matrix. Numerous oval structures (< 1.5 mm in diameter), most likely amygdoidal vesicles filled with authigenic minerals, are dispersed pervasively in the rock. They contain carbonates (calcite, Fe-dolomite/ankerite, siderite, and magnesite), fibrous-radial silica (tridimite according to XRD; Fig. 5), and barite. The rock appears to be stained with a ferruginous material.

PdV-1 and PdV-6 are metasedimentary rocks, metapsamite and metapelite, respectively. PdV-1 (Fig. 9C) is weakly laminated, with framework grains dominated by quartz and relatively coarse-grained colorless detrital mica, with individual zircon, rutile, tourmaline, and opaque grains. The intergranular spaces are filled with fine-grained colorless illite and authigenic calcite. PdV-6 (Fig. 9D) is massive and also dominated by quartz and colorless mica (coarse flakes) and illite (fine grained flakes in pore space).

CT-4 is an altered tuffite with a brecciated texture (Fig. 9E, F). The main components are fine-grained quartz and fine colorless mica – most probably illite based on XRD data. Individual

https://doi.org/10.1180/clm.2025.10014 Published online by Cambridge University Press

outsized mica flakes represent the detrital material. Authigenic silica and carbonates occur in isolated domains.

K-Ar dating of clay fractions

All fractions of the Port de Valldemossa samples gave K-Ar ages younger than the Triassic stratigraphic age (Table 3). The PdV-1 ages decrease gradually with clay fraction from 230 to 186 Ma. The PdV-6 sample gave oldest age of the coarsest fraction (216 Ma), while youngest age (184 Ma) in the middle fraction. K-Ar ages of the PdV-7 fractions are equal within the experimental error (133-140 Ma). K-Ar ages of the Cala Tuent sample (CT-4) decrease with grain size from 235 Ma (equal or slightly older than the stratigraphic age) to 175 Ma.

Chemical analyses of PdV-7 illite

Petrographic observations identified in the PdV-7 sample three morphological varieties of illite: illitic matrix, illite pseudomorphs after feldspar, and after biotite (Fig. 9A, B). Their microprobe analyses are presented in Table 4, along with the calculated structural formulae. Ti was not included in the formula calculation, as abundant anatase was detected in this sample (Fig. 5 and 7) and Fe was regarded as trivalent. PdV-7/11 analysis gave too low octahedral cations, which was corrected by assuming quartz contamination and decreasing SiO_2 to 52 %. All analyses of altered biotite have octahedral cations above 2.00, indicating some remnants of the trioctahedral structure, but only trivalent iron. Based on these analyses, the mineral replacing feldspar can be classified as illite, the matrix mineral as mixed-layer illite-smectite, and the mineral replacing biotite as close to ferromuscovite (ferrimuscovite), i.e. intermediate between muscovite and celadonite (Rieder *et al*., 1999).

https://doi.org/10.1180/clm.2025.10014 Published online by Cambridge University Press

INTERPRETATION

Diagenetic/metamorphic grade

Traces of swelling detected in all illites, indicative of <10% of swelling layers, identify our samples as representing the maximum paleotemperatures higher than 180 ^{o}C (Środoń, 2007) but much lower than 250-275 ^{o}C, i.e. the temperature of illite swelling disappearance (McDowell & Elders, 1980; Akker et al., 2021). Ir values indicate diagenesis/anchizone boundary temperatures (Bozkaya *et al*., 2016, 2021). This is consistent with the lack of $2M_1$ illite in sample PdV-7, which does not contain the detrital components: the temperatures were too low for the crystallization of authigenic $2M_1$ illite, which appears at temperatures close to the onset of anchizone (c. 200 ^{o}C; Frey & Robinson, 1999, their Fig. 2.1). The Kubler index values, which were measured for shales and a tuff (Table 1), are above 0.52 °2θ CuK_{α}, i.e. above the standardized diagenesis/anchizone boundary value (Warr & Ferreiro-Mählmann, 2015), thus they indicate deep diagenetic conditions, below 200 °C.

The presented maximum paleotemperature evaluation is based on the published data sets measured for shales and bentonites. Commonly, bentonites produce slightly lower estimates of the maximum paleotemperatures than the surrounding shales (e.g. Šucha et al., 1993). It is interpreted as an indication of the deficit of potassium in bentonites, which has to be imported from shales, as evidenced best by rare cases of the zonation of illitization in bentonites (Środoń, 1976; Altaner et al, 1984), but also paleosols (Liivamägi et al., 2021). The thick detrital illite in shales may also contribute to this effect. The effect is visible in our data set, but it is very small: PdV-7 sample (the volcanic rock) has slightly more expandability (Fig. 6) and higher Ir index (Table 1) than sedimentary samples (volcanoclastics). Also within sample PdV-7 we observe

https://doi.org/10.1180/clm.2025.10014 Published online by Cambridge University Press

variation of expandability, evidenced by variable interlayer cation contents (Table 4): from 0.56-0.62/$O_{10}(OH)_2$ in the illitic matrix to 0.84-0.86 in the illitic pseudomorphs after K-feldspar. These values correspond to c. 16-<5 %S (Środoń et al., 2009a). Our data document that, at such temperature range (c. 180-200 °C), illite chemistry is controlled by the chemistry of precursor material, but the availability of potassium in these rocks is of secondary importance when evaluating the maximum paleotemperatures.

Age of the authigenic illite

Three samples containing mixtures of illite polytypes provided the highest K-Ar dates for the coarsest fractions, with the most abundant $2M_1$ illite/mica. Such relationship and the lack of $2M_1$ illite/mica in the sample PdV-7 indicate that the $2M_1$ polytype is a detrital mica (Środoń *et al*., 2002). This conclusion is consistent with the petrographic observations, which document abundant detrital mica and quartz in all samples containing the $2M_1$ polytype (Fig. 9C-F). Thus the dates of such samples are mixed ages between the age of detrital $2M_1$ mica and the age of authigenic $1M/1M_d$ illite. These data allow to conclude that the illite authigenesis took place after the youngest date of these samples (< 175 Ma).

Petrographic observations imply that the PdV-7 sample represents deeply altered (sub)volcanic rock without detrital contamination. The ages of all three fractions of the PdV-7 sample, equal within the analytical error, and the lack of detectable $2M_1$ contamination allow to conclude that the authigenic illite in these rocks crystallized between 140 and 133 Ma, i.e. during Early Cretaceous, before the Barremian. The sequence of ages (oldest in the finest fraction, and intermediate in the coarsest fraction, which typically contains aggregates and not individual crystals, dominating in finer fractions) probably reflects a several million years duration of illite

https://doi.org/10.1180/clm.2025.10014 Published online by Cambridge University Press

crystallization and growth (finest crystals are first to form: Środoń *et al*., 2002). Such estimation of the age of authigenic illite is confirmed by plotting the exp(λt-1) and K-Ar ages of size fractions of sample PdV-1 (Fig.10) against the percentage of detrital K ($\%I_{d(K)}$ – see definition in Szczerba & Środoń, 2009). The plot is linear and it extrapolates to c. 135.4 ± 15.7 (2σ) Ma for 0 % $2M_1$ (only $1M+1M_d$ present), and to c. 340.0 ± 28.5 (2σ) Ma (Variscan metamorphism) for 100% $2M_1$. The closest known major source of the Variscan metamorphic rocks is the Betic Cordillera (Martín-Algarra et al., 2019), but even in Serra de Tramuntana small outcrops of the metamorphosed Carboniferous sediments are present (Fornos & Gelabert, 1995).

Origin of the authigenic Early Cretaceous illite

Our data indicate that the authigenic illite crystallized in the Triassic rocks of Serra de Tramuntana, both volcanic (PdV-7) and volcano-sedimentary (PdV-1), in the Lower Cretaceous, thus c. 100 Ma after deposition, at temperatures close but below the diagenesis/anchimetamorphism boundary (180-200 ^{o}C). The illitization process is then unrelated to the contact metamorphism or alteration of hot volcanics by post-magmatic fluids or seawater (spilitization). Tectonic models assume that the Triassic to Lower Cretaceous rocks of Mallorca were essentially flat-lying until the Late Oligocene, when thrusting and folding, responsible for the present-day tectonic structure started (Gelabert *et al*., 2004, Fig. 9; Sábat *et al*., 2011, Fig. 18). Thus illitization cannot be explained by the tectonic burial. Pre-tectonic sedimentary burial diagenesis in common geothermal regime can be excluded also, as the maximum thickness of the entire Triassic to Lower Cretaceous sedimentary section does not exceed 1500 m (Fig. 1), thus burial under common geothermal gradient conditions (20-40 ^{o}C/km) could provoke at most the incipient illitization of smectite.

https://doi.org/10.1180/clm.2025.10014 Published online by Cambridge University Press

At the time of illite crystallization, the Lower Cretaceous sediments of Mallorca indicate deep sea conditions. The area was uplifted and eroded in the Upper Cretaceous, and this radical change from extensional to contractional regime (Moragues *et al*., 2021), known from much broader area around, is interpreted as the onset of convergence between Africa and Europe (Ramos-Guerrero *et al*., 1989; Schettino & Turco, 2011). Assuming that all these tectonic models are correct, the only feasible scenario explaining the detected level of illitization is a very high geothermal gradient related to thinning of the crust at the end of the Cretaceous extensional phase, even more extreme than known today from the Pannonian Basin (c. 80 ^{o}C/km: Lenkey *et al*., 2002), and possibly related hydrothermal activity. Analogous shallow burial Mesozoic thermal event, produced by rifting and lithospheric thinning, is known in Europe between the Paris Basin and the North Sea and the Upper Silesia Coal Basin. It was originally postulated by Bonhomme (1982) and then confirmed by numerous studies (cf. references and discussion in Środoń et al., 2009b).

Thee Lower Cretaceous age of illitization implies that the Alpine thrusting and folding in Serra de Tramuntana affected rocks which were already strongly altered, and that the Alpine phase maximum paleotemperatures in Serra de Tramuntana were below 200 ^{o}C, as the Cretaceous characteristics of illite have not been changed. This conclusion applies to the entire Mallorca, as our samples were collected from the bottom of the nappe stack (Gelabert *et al*., 2004, Fig. 9; Sábat *et al*., 2011, Fig. 18).

Implications for the tectonic history of Mallorca

The Balearic Islands are considered as the emerged parts of Balearic Promontory, i.e. the offshore prolongation of the External Zones of the Betic Cordillera in Spain (e.g.. Vergés et al.,

https://doi.org/10.1180/clm.2025.10014 Published online by Cambridge University Press

2019, their fig. 1.3). Diagenetic/metamorphic events affecting the Triassic rocks of Betic Cordillera have been extensively studied only in the Internal Zone (summaries in Nieto *et al*., 2019 and Garrido *et al*., 2019). The level of alteration of the Triassic rocks of the Maláguide and Alpujárride complexes range from the late diagenesis to epimetamorphism. Pyrophyllite, paragonite, and chloritoid detected in some of these rocks (Ruiz Cruz *et al*., 2005) indicate anchizonal/epizonal temperatures. All available radiometric dates of these metamorphosed sediments and the K-Ar dates of the Triassic basic intrusions (Puga and Torres-Roldán, 1989) indicate the Alpine age of these alterations, supported by the subsidence analysis (Perri *et al*., 2013).

Published information on the level of diagenesis/metamorphism of the External Zone sedimentary rocks (mostly marls) is lacking. The External Zone sediments host abundant mafic tectonic blocs (called "ophites"), intrusions, and pillow lavas, ranging in age from the Late Triassic to the Early Cretaceous. Their secondary mineral composition: (prehnite, pumpellyite, actinolite, chlorite, illite, zeolites) indicates low-grade metamorphism (Puga et al., 1988; Morata et al., 1997). The whole-rock K-Ar ages, mostly younger than the stratigraphic ages, support massive alteration of the igneous rocks and go down to 48 Ma (Puga et al., 1988), indicating, at least locally, an effect of the Alpine metamorphism, which has not been detected in Mallorca. It remains to be investigated if this Alpine metamorphism overprinted the Early Cretaceous alteration of the External Zone rocks, analogous to the alteration detected in Mallorca.

According to Bourrouilh (2016), "the history of the Balearic archipelago seems to be closer to the tectonic opening of the Gulf of Valencia and to the Corsica-Sardinia rotation, and thus to the tectonic history of the Western Mediterranean Sea, than to the tectonics of the Betic Cordillera". Zircon fission track analyses from the Variscan basement of Corsica yield ages

https://doi.org/10.1180/clm.2025.10014 Published online by Cambridge University Press

between 144.6 ± 10 and 159.2 ± 9.8 Ma. These ages are interpreted as a record of a thermal event related to the Jurassic opening of the Ligurian-Piedmont Ocean (Danišík, 2005), thus perhaps they document an earlier phase of the same event as our K-Ar dates from Mallorca. According to Dercourt *et al*. (1986), this Jurassic-Cretaceous extension, involving Africa and Europe, produced a continuous oceanic corridor from the Gulf of Mexico to Tibet.

CONCLUSIONS

1. Only one sample among 15 collected turned out to be a volcanic rock without detrital contamination.
2. This sample, containing only $1M+1M_d$ illite polytypes, gave the K-Ar ages of three clay fractions from 133 to 140 Ma, thus identical within the experimental error, and interpreted as the age of illitization (Valanginian).
3. Samples contaminated with the $2M_1$ detrital polytype gave K-Ar ages decreasing with grain fraction from 235 Ma (c. stratigraphic age) to 175 Ma, interpreted as mixed detrital/authigenic ages.
4. Polytype extrapolations to 0% of $2M_1$ confirm that the $1M+1M_d$ illite polytypes are of Early Cretaceous age (135 Ma), and the $2M_1$ polytype is detrital of the Variscan age (c. 340 Ma).
5. Mineralogical characteristics of illite, including Kubler index measured on Ca-exchanged <2 μm fractions of shale samples, identify the maximum palotemperatures experienced by the Triassic rocks at the bottom of Serra de Tramuntana nappe stack as close but below the diagenesis/anchizone boundary (180-200 ^{o}C).

https://doi.org/10.1180/clm.2025.10014 Published online by Cambridge University Press

6. Such paleotemperatures were attained by tectonically undeformed Triassic sedimentary rocks under not more than 1500 m of overburden, thus they are interpreted as reflecting an extreme geothermal gradient at the end of the Mesozoic extension of the area.
7. These non-reset Cretaceous ages and illite characteristics identify the Cenozoic tectonic burial temperatures in Mallorca as lower than c. 200 ^{o}C.
8. Illites crystallized at the estimated paleotemperatures preserve chemical variation reflecting their origin from different parent materials.

ACKNOWLEDGEMENTS

MS acknowledges financial support from the NCN (Polish National Science Centre): OPUS 2020/37/B/ST10/01697 for the K-Ar measurements. Fernando Nieto and Laurence Warr reviewed our paper very thoroughly, offering many valuable and inspiring suggestions.

Competing interests: The authors declare none.

REFERENCES

Akker I.V., Berger A., Zwingmann H., Todd A., Schrank C.E., Jones M.V.M., Kewish C.M.,Schmid T.C. & Herwegh M. (2021) Structural and chemical resetting processes in white mica and their effect on K-Ar data during low temperature metamorphism. *Tectonophysics*, **800**, 228708.

Altaner S.P., Hower J., Whitney G. & Aronson J.L. (1984) Model for K-bentonite formation: Evidence from zoned K-bentonites in the disturbed belt, Montana. *Geology*, **12**, 412–415.

Bonhomme M.G. (1982) Age triasique et jurassique des argiles associées aux minéralisations filoniennes et de phénoménes diagénétiques tardifs en Europe de l'Ouest. Contexte

https://doi.org/10.1180/clm.2025.10014 Published online by Cambridge University Press

géodynamique et implications génétiques. *Comptes Rendus de l'Académie des Sciences*, **304**, 521–524.

Bourrouilh R. (2016) The Balearic Islands in the Alpine Orogeny. *Boletín Geológico y Minero*, **127**, 527–546.

Bozkaya Ö., Bozkaya G., Uysal T. & Banks D.A. (2016) Illite occurrences related to volcanic-hosted hydrothermal mineralization in the Biga Peninsula, NW Turkey: Implications for the age and origin of fluids. *Ore Geol. Rev.*, **76**, 35–51.

Bozkaya Ö., Günal-Türkmenoğlu A., Göoncüoğlu M.C., & Okuyucu C. (2021) Geological, mineralogical and geochemical characteristics of Mississippian K-bentonites from southern Turkey: A correlation with coeval tephras from Gondwana-derived terranes. *J. African Earth Sci.*, **181**, 104258.

Danišík M. (2005) *Cooling history and relief evolution of Corsica (France) as constrained by fission track and (U-Th)/He thermochronology*. PhD thesis, Universität Tübingen, Germany.

Dercourt J., Zonenshain L.P., Ricou L.E., Kazmin V.G., Le Pichon X., Knipper A.L., Grandjacquet C., Sortshikov I.M., Geysant J., Lepvrier C., Pechersky D.H., Boulin J., Sibuet J.C., Savostin L.A., Sorokhti, O., Westphal M., Bazhenov M.L., Lauer J.P. & Biju-Duval B. (1986) Geological evolution of the Tethys belt from the Atlantic to the Pamir since Lias. *Tectonophysics*, **123**, 241–315.

Enrique P. (1986) Nota sobre les roques hipabissals de la Serra de Tramuntana de Mallorca: algunes característiques petrográfiques i geoquímiques. *Boll. Soc. Hist. Nat. Balears*, **30**, 19–50.

https://doi.org/10.1180/clm.2025.10014 Published online by Cambridge University Press

Enrique, P. (2012) Rocas teschenítica en el Norte de Mallorca: aproximación a su clasificación. *Geogaceta*, **51**, 11–14.

Enrique P. (2016) Las rocas básicas alcalinas intrusivas del Norte de Mallorca (Islas Baleares): características geoquímicas. *Geogaceta*, **59**, 71–74.

Fornós J.J. & Gelabert B. (1995) Lithology and tectonics of the Majorcan karst. *Mon. Soc. Hist. Nat. Balears*, **3**, 27–43.

Frey M. & Robinson D. (1999) *Low-Grade Metamorphism.* Blackwell Science, 313 pp.

Garrels R.M. & Mackenzie F.T. (1971) *Evolution of Sedimentary Rocks*. Norton, New York, 397 pp.

Garrido C.J., Acosta-Vigil A., Barich A. & Hidas, K. (2019) Metamorphism of the Alpujárride Complex. Chapter 13.2 in: *The Geology of Iberia: A Geodynamic Approach: Volume 3: The Alpine Cycle* (C. Quesada and J.T. Oliveira, editors). Springer.

Gelabert B., Sàbat F., Hardy S. & Rodríguez-Perea A. (2004) Significance of inherited normal faults during inversion tectonics: an example from the Tramuntana Range, Mallorca, *Geodinamica Acta*, **17**, 363–373.

Hoffman J. & Hower J. (1979) Clay mineral assemblages as low grade metamorphic geothermometers: application to the thrust faulted disturbed belt of Montana, U.S.A. *SEPM Special Publication*, **26**, 55–79.

Hunziker J.C., Frey M., Clauer N., Dallmeyer R.D., Friedrichsen H., Flehmig W., Hochstrasser K., Roggwiler P. & Schwander H. (1986) The evolution of illite to muscovite: mineralogical and isotopic data from the Glarus Alps, Switzerland. *Contrib. Mineral. Petrol*., **92**, 157–180.

https://doi.org/10.1180/clm.2025.10014 Published online by Cambridge University Press

Jackson M.L. (1975) *Soil Chemical Analysis – Advanced Course* (2nd ed.), published by the author, Madison, Wisconsin.

Kübler B. (1968) Évaluation quantitative du métamorphisme par la cristallinité del'illite; état des progress realisés ces dernières années. *Bull. Cent. Rech. Pau (Soc. Nat. Pet. Aquit.),* **2**, 385–397.

Lenkey L., Dövényi P., Horváth F. & Cloetingh S.A.P.L. (2002) Geothermics of the Pannonian basin and its bearing on the neotectonics. *European Geosciences Union Stephan Mueller Special Publication Series*, **3**, 29–40.

Liivamägi S., Środoń J., Bojanowski M.J., Stanek J.J. & Roberts, N.M.W. (2021) Precambrian paleosols on the Great Unconformity of the East European Craton: an 800 million year record of Baltica's climatic conditions. Precambrian Research, **363**, 106327

Martín-Algarra, A. et al. (2019). Paleozoic Basement and Pre-Alpine History of the Betic Cordillera. In: *The Geology of Iberia: A Geodynamic Approach. Regional Geology Reviews* (C. Quesada & J. Oliveira, editors). Springer, Cham.

McDowell S.D. & Elders W.A. (1980) Authigenic layer silicate minerals in borehole Elmore 1, Salton Sea Geothermal Field, California, USA. *Contrib. Mineral. Petrol*., **74**, 293–310.

Moragues L., Ruano P., Azañón J. M., Garrido C. J., Hidas K., & Booth Rea G. (2021) Two Cenozoic extensional phases in Mallorca and their bearing on the geodynamic evolution of the Western Mediterranean. *Tectonics*, **40**, e2021TC006868.

Navidad M. & Alvaro M. (1985) El vulcanismo alcalino del Triásico Superior de Mallorca (Mediterráneo Occidental). *Boletín Geológico y Minero*, **96**, 10–22.

https://doi.org/10.1180/clm.2025.10014 Published online by Cambridge University Press

Nieto F, Abad I, & Velilla N. (2019) Metamorphism of the Maláguide Complex. Chapter 13.1 in: *Regional Geology Reviews. The Geology of Iberia: A Geodynamic Approach: Volume 3: The Alpine Cycle (*C. Quesada and J.T. Oliveira, editors). Springer.

Perri F., Critelli S., Martín-Algarra A., Martín-Martín M., Perrone V., Mongelli G. & Zattin M. (2013) Triassic redbeds in the Malaguide Complex (Betic Cordillera — Spain): Petrography, geochemistry and geodynamic implications. *Earth-Science Reviews*, **117**, 1–28.

Puga E. & Torres-Roldán R.L. (1989) Geochemistry and age relationships of metamorphosed mafic sills from Sierra de Enmedio and Sierra de Carrascoy (Eastern Betic Zone, southeastern Spain). *Estudios geol.*, **45**, 325–336.

Ramos-Guerrero E., Rodriguez-Perea A., Sàbat F. & Serra-Kiel J. (1989) Cenozoic tectosedimentary evolution of Mallorca island. *Geodinamica Acta*, **3**, 53–72.

Rieder M., Cavazzini G., D'yakonov Yu.S., Frank-Kamenetskii V.A., Gottardi G., Guggenheim S., Koval' P.V., Müller G., Neiva A.M.R., Radoslovich E.W., Robert J.-L., Sassi F.P., Takeda H., Weiss Z. & Wones D.R. (1999) Nomenclature of the micas. *Mineralogical Magazine*, **63**, 267–279.

Ruiz Cruz M.D., Sanz de Galdeano C. & Lázaro C. (2005) Metamorphic evolution of Triassic rocks from the transition zone between the Maláguide and Alpujárride complexes (Betic Cordilleras, Spain). *Eur. J. Mineral.*, **17**, 81–91.

Sàbat F., Gelabert B., Rodríguez-Perea A. & Giménez J. (2011) Geological structure and evolution of Majorca: Implications for the origin of the Western Mediterranean. *Tectonophysics*, **510**, 217–238.

https://doi.org/10.1180/clm.2025.10014 Published online by Cambridge University Press

Schettino A. & Turco E. (2011) Tectonic history of the western Tethys since the Late Triassic. *GSA Bull*., **123**, 89-105.

Szczerba M. & Środoń J. (2009) Extraction of diagenetic and detrital ages and of the $^{40}K_{detrital}/^{40}K_{diagenetic}$ ratio from K-Ar dates of clay fractions. *Clays and Clay Minerals*, **57**, 93–103.

Środoń J. (1976) Mixed-layer smectite/illites in the bentonites and tonsteins of the Upper Silesian Coal Basin. *Prace Mineralogiczne*. **49**, 84 pp.

Środoń J. (1984) X-ray powder diffraction identification of illitic materials. *Clays and Clay Minerals*, **32**, 337–349.

Środoń J. (2007) Illitization of smectite and history of sedimentary basins. Pp.74–82 in: *Invited Lectures, EUROCLAY 2007* (F. Rocha, D. Terroso & A. Quintela, editors). Aveiro, Portugal.

Środoń J. (2025) The role of illite in the global cycle of elements. *Clays and Clay Minerals,* **73** (in press).

Środoń J. & Jewuła K. (2025) Controls over cesium and rubidium contents of sedimentary rocks. *Chemical Geology*, **683**, 122745.

Środoń J., Clauer N. & Eberl D.D. (2002) Interpretation of K–Ar dates of illitic clays from sedimentary rocks aided by modelling. *Am. Mineral*., **87**: 1528–1535.

Środoń J., Clauer N., Banaś M. & Wójtowicz A. (2006) K-Ar evidence for a Mesozoic thermal event superimposed on burial diagenesis of the Upper Silesia Coal Basin. *Clay Minerals,* **41**, 671–692.

https://doi.org/10.1180/clm.2025.10014 Published online by Cambridge University Press

Środoń J., Zeelmaekers E. & Derkowski A. (2009) The charge of component layers of illite-smectite in bentonites and the nature of end-member illite. *Clays and Clay Minerals*, **57**, 649–671.

Środoń J., Williams L., Szczerba M., Zaitseva T., Bojanowski M., Marciniak-Maliszewska B., Ciesielska Z. & Paszkowski M. (2023) Mechanism of late diagenetic alteration of glauconite and implications for geochronology. *Geochim. Cosmochim. Acta*, **352**, 157–174.

Šucha V., Kraus I., Gerthofferova H., Petes J. & Serekova M. (1993) Smectite to illite conversion in bentonites and shales of the East Slovak Basin. *Clay Minerals*, **28**, 243–253.

Ufer K., Kleeberg R., Bergmann J. & Dohrmann R. (2012) Rietveld refinement of disordered illite-smectite mixed-layer structures by a recursive algorithm. II: Powder-pattern refinement and quantitative phase analysis. *Clays and Clay Minerals*, **60**, 535–552.

Vergés J., Kullberg J.C., Casas-Sainz A., de Vicente G., Duarte L.V., Fernàndez M., Gómez J.J., Gómez-Pugnaire M.T., Sánchez A.J., López-Gómez J., Macchiavelli C., Martín-Algarra A., Martín-Chivelet J., Muñoz J.A., Quesada C., Terrinha P., Torné M. & Vegas R. (2019) An Introduction to the Alpine Cycle in Iberia. Chapter 1 in: *The Geology of Iberia: A Geodynamic Approach: Volume 3: The Alpine Cycle (*C. Quesada and J.T. Oliveira, editors). Springer.

War L.N. & Ferreiro-Mählmann R. (2015) Recommendations for Kübler Index standardization. *Clay Minerals*, **50**, 282–285.

Warr L.N. (2018) A new collection of clay mineral ‘Crystallinity’ Index Standards andrevised guidelines for the calibration of Kübler and Árkai indices. *Clay Minerals*, **53**, 339–350.

https://doi.org/10.1180/clm.2025.10014 Published online by Cambridge University Press

Warr L.N. (2022) Earth's clay mineral inventory and its climate interaction: A quantitative assessment. *Earth-Science Reviews*, **234**, 104198

Figure and table captions

FIG. 1. Synthetic lithostratigraphic column of Mallorca (after Fornos & Gelabert, 1995).

Fig. 2. Localization of all samples on the topographic maps (mapy.com) of Port de Valldemossa (a) and Cala Tuent (b).

Fig. 3. Localization of most samples (their macroscopic identification in Table 1) on photographs. A – SW shore of Port de Valldemossa; B – NE shore of Port de Valldemossa, C – detail localization of sample PdV-7; D – road cut at Cala Tuent, E – detail localization of sample CT-8 in the road cut at Cala Tuent; F – detail localization of samples CT-4 and CT-5 west of the Cala Tuent beach.

FIG. 4. Representative bulk rock random XRD patterns of the Cala Tuent samples. Q – quartz, B – barite, An – anatase, Tr – tridimite, D – dolomite, ZnO – internal standard, Sp – sphalerite (?), Dw – dawsonite, 2M1 – $2M_1$ illite/mica, Rt – rutile, H – hematite.

FIG. 5. Representative bulk rock random XRD patterns of the Port de Valldemossa samples. 1M – 1M illite, Q – quartz, Pl – plagioclase, C – calcite, Py – pyroxene, ZnO – internal standard, Ch – chlorite, An – anatase, 2M1 – $2M_1$ illite/mica, D – dolomite, Or – orthoclase, H – hematite.

FIG. 6. XRD patterns of oriented air-dry and glycolated 2-0.5 μm fractions of samples selected for K-Ar dating. Ir – degree of swelling index of Środoń (1984), Ch – chlorite, Q – quartz. Illite reflections marked with their 00l indices.

https://doi.org/10.1180/clm.2025.10014 Published online by Cambridge University Press

FIG. 7. XRD patterns of random fractions of two samples selected for K-Ar dating, illustrating differences in illite polytype composition and relative concentrations of illite and illite-smectite in fractions of sample PdV-7, visible in 001 region. Dw – dawsonite, Q – quartz, Rt – rutile, An – anatase, Fa – fluoroapatite, H – hematite.

FIG. 8. Results of illite polytype quantification from XRD patterns of three random fractions of sample PdV-1.

FIG. 9. Plane polarized (PPL) and cross-polarized (XPL) microphotographs of samples selected for K-Ar dating. (A – PPL and B – XPL) paired images of sample PdV-7, deeply altered subvolcanic rock with diabasic texture. Note oval structures filled with carbonates (carb) and tridimite (SiO_2). Arrows indicate examples of lath-shaped former feldspars currently replaced by illite. (C) XPL image of sample PdV-1, metapsamite with authigenic calcite (cal) and two populations of colorless mica: coarse detrital grains and fine-crystalline masses filling intergranular porosity (indicated with arrows). (D) XPL image of sample PdV-6, metapelite with two populations of colorless mica: coarse detrital grains and fine-crystalline masses. (E) XPL image of sample CT-4, tuffite with brecciated texture and with authigenic calcite (cal). (F) higher-magnification XPL image of sample CT-4 showing two populations of colorless mica: coarse detrital grains and fine-crystalline masses (indicated with arrows).

FIG. 10. K-Ar ages and exp(λt-1) vs. % K in the $2M_1$ polytype ($\%I_{d(K)}$ – according to the equation by Szczerba & Środoń, 2009). $\%I_{d(K)}$ were calculated from the percentages of K in the end member phases estimated from the extrapolation of % K to 0% and 100% of $2M_1$ polytype. The results are: 7.8 and 6.8 %, for $2M_1$ and 1Md+1M, respectively. Confidence bands were

https://doi.org/10.1180/clm.2025.10014 Published online by Cambridge University Press

calculated using Monte Carlo method. Error bars corresponds to 2σ, assuming ±1.5% uncertainity in the detrital potassium estimate.

TABLE 1. Localization, field identification, and stratigraphic position of all collected samples, Kubler index, and Ir index of Środoń (1984) of selected samples.

TABLE 2. Results of quantitative mineralogical analyses for clay fractions of sample PdV-1 including illite polytype quantification.

TABLE 3. K-Ar data for illite in clay fractions, stratigraphic positions of samples, and d_{060} of illite in these fractions.

TABLE 4. EPMA chemical analyses of different types of illite in sample PdV-7 (in wt. %), along with structural fromulae calculated from these analyses (for PdV-7/11 also corrected for the admixture of quartz).

https://doi.org/10.1180/clm.2025.10014 Published online by Cambridge University Press

Figure 1

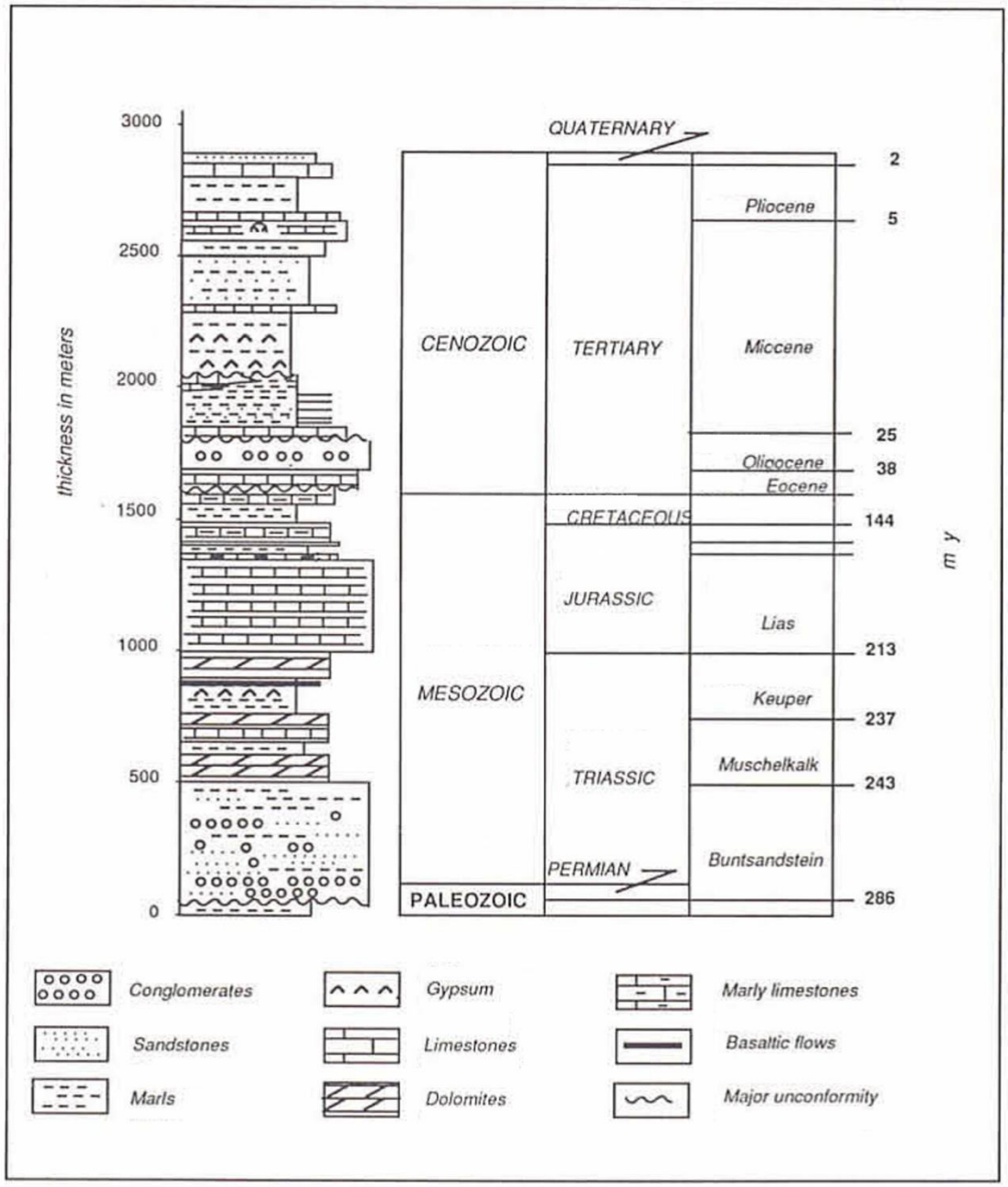

https://doi.org/10.1180/clm.2025.10014 Published online by Cambridge University Press

Figure 2

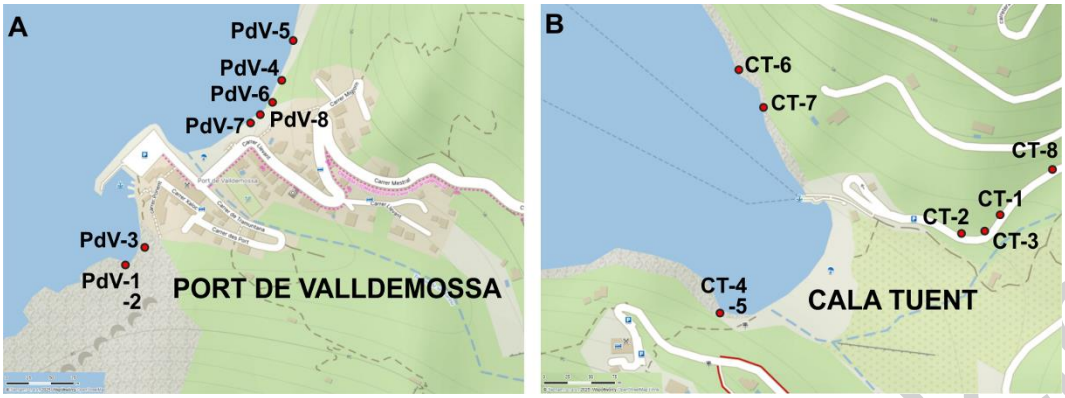

Figure 3

https://doi.org/10.1180/clm.2025.10014 Published online by Cambridge University Press

Figure 4

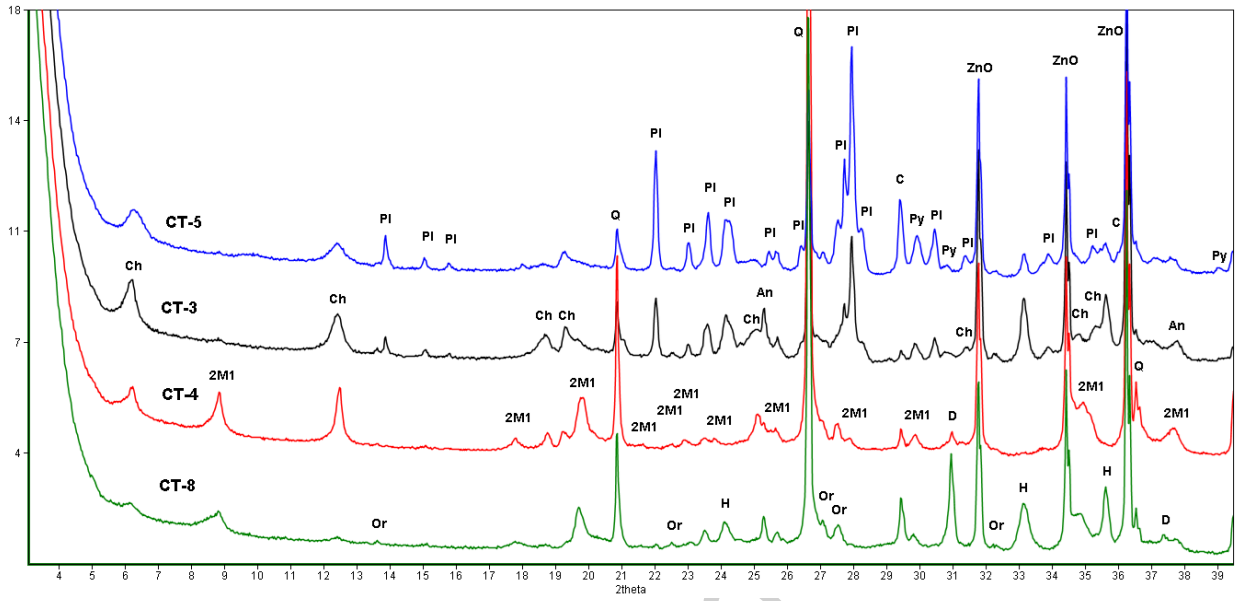

Figure 5

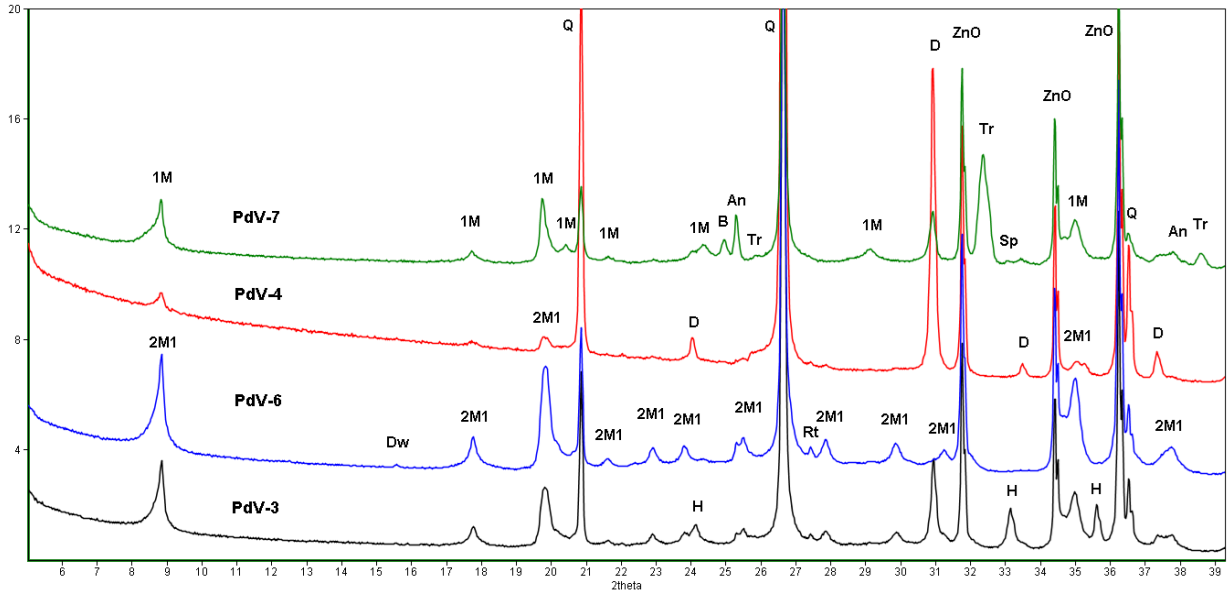

https://doi.org/10.1180/clm.2025.10014 Published online by Cambridge University Press

Figure 6

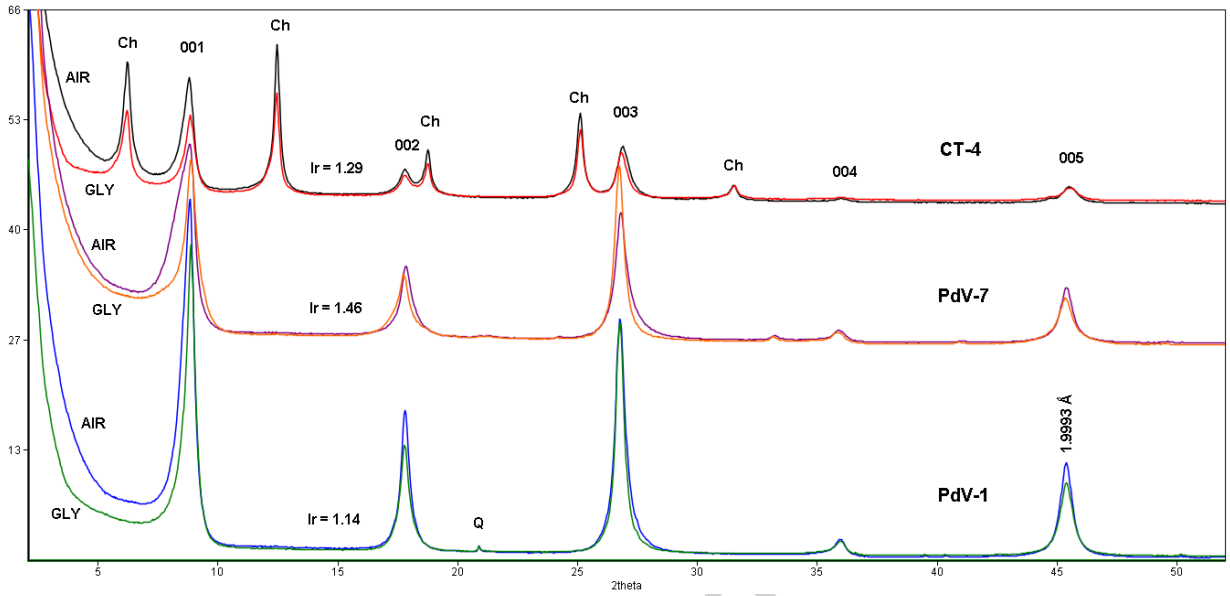

Figure 7

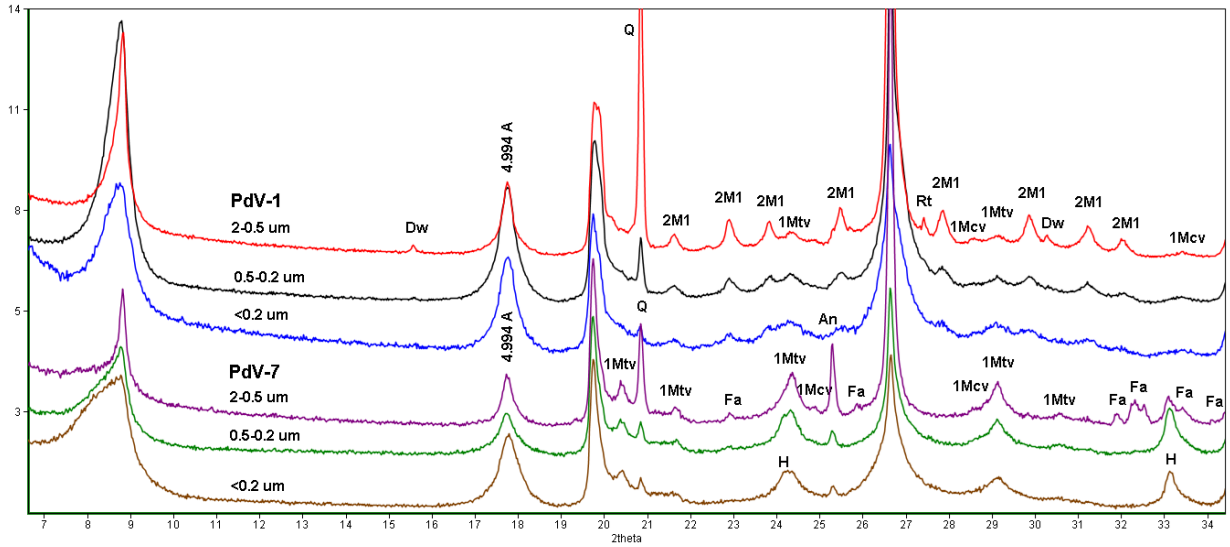

https://doi.org/10.1180/clm.2025.10014 Published online by Cambridge University Press

Figure 8

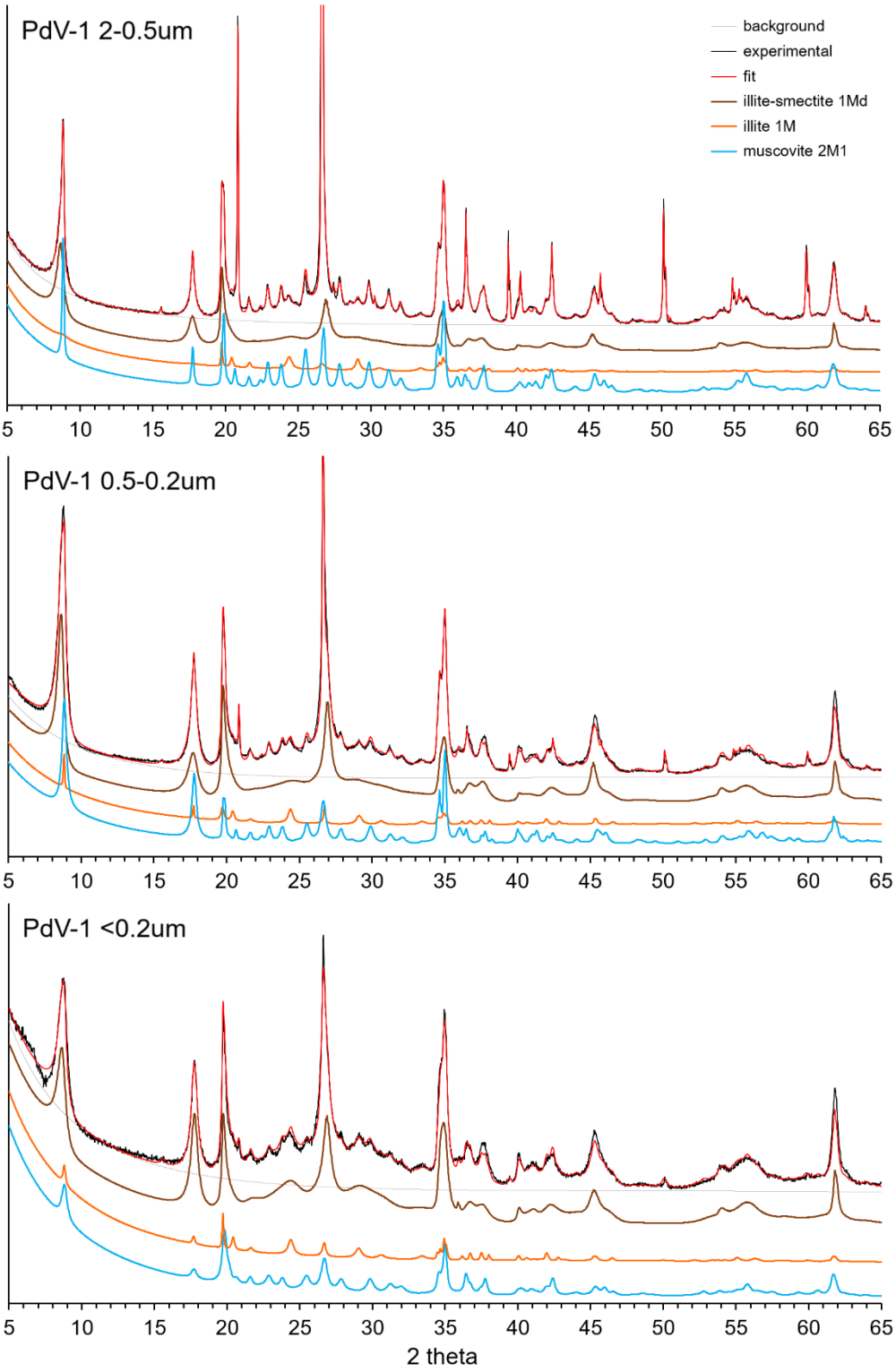

https://doi.org/10.1180/clm.2025.10014 Published online by Cambridge University Press

Figure 9

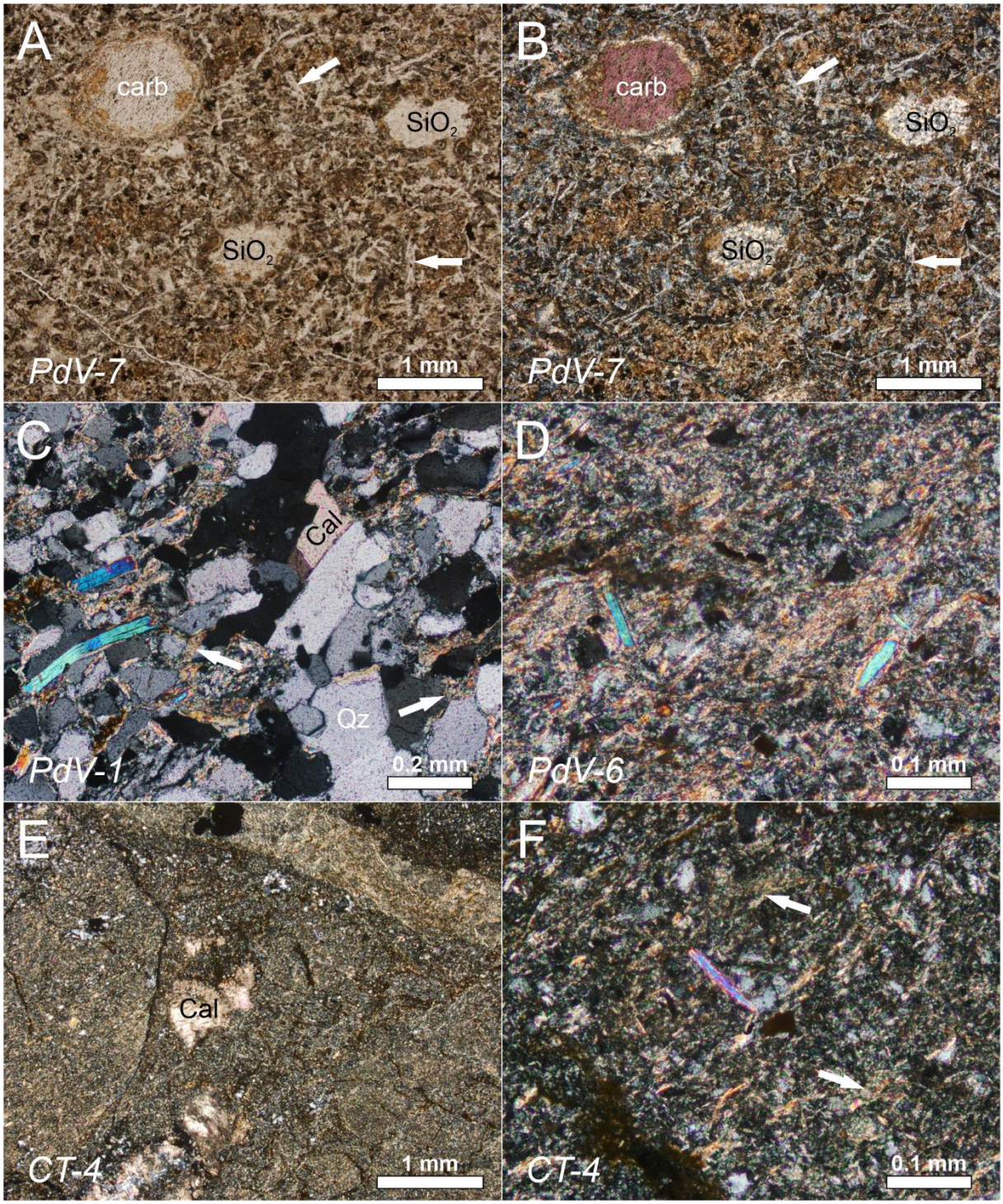

https://doi.org/10.1180/clm.2025.10014 Published online by Cambridge University Press

Figure 10

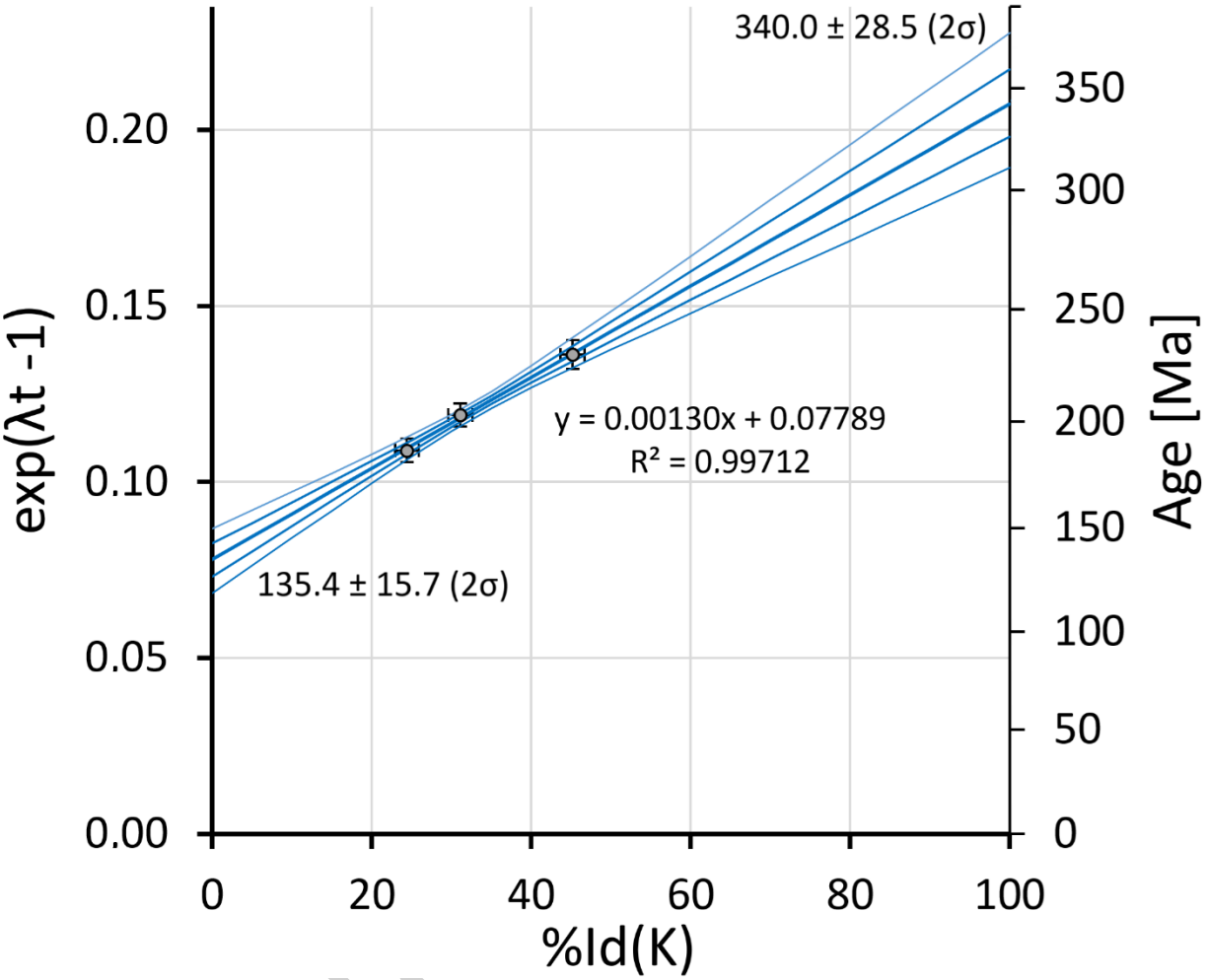

https://doi.org/10.1180/clm.2025.10014 Published online by Cambridge University Press

Table 1

Sample No.	Field identification and localization	Stratigraphy	Kubler index [°2θ CuK$_\alpha$]	Ir index
Port de Valldemossa		Buntsandstein		
SW of port				
PdV-1	volcanics c. 100 m from port			1.14
PdV-2	volcanics c. 100 m from port			
PdV-3	red shale 40 m from volc. towards port		0.7	
NE of port				
PdV-4	volcanics c. 200 m from port			
PdV-5	red shale 5 m behind volcanics		0.74	
PdV-6	contact of volcanics			
PdV-7	thin yellow volcanic layer			1.46
PdV-8	main volcanics closer to port			
Cala Tuent		Keuper		
by the road				
CT-1	massive volcanics at road turn			
CT-2	massive volcanics at road turn			
CT-3	massive volcanics at road turn			
CT-8	red shale 70 m E of volcanics		1.03	
W of port				
CT-4	soft clay (tuff?) c. 50 m from beach		0.71	1.29
CT-5	massive volcanics above CT-4			
E of port				
CT-6	brittle volcanics c. 150 m from port			
CT-7	massive volcanics c. 100 m from port			

https://doi.org/10.1180/clm.2025.10014 Published online by Cambridge University Press

Table 2

Sample	Quartz	Illite $2M_1$	Illite 1M	Illite $1M_d$	Rutile	Dawsonite	Zircon	SUM
PdV-1 2–0.5 μm	24.6	31.3	7.2	35.9	0.6	0.4	0.1	100.0
PdV-1 0.5–0.2 μm	6.0	26.5	6.9	60.0	0.3	0.3	0.0	100.0
PdV-1 <0.2 μm	5.0	21.0	8.0	65.5	0.4	0.1	0.0	100.0

Table 3

Sample	% K_2O	Mass [mg]	% $^{40}Ar^*$	Age [Ma]	2σ error	Strat. age	d_{060}
PdV-1 2-0.5 um	6.486	13.69	90.2	230.31	6.92	Buntsandstein	1.5003
PdV-1 0.5-0.2 um	7.872	19.27	95.1	202.87	5.46	246 - 251 Ma	1.5003
PdV-1 <0.2 um	8.021	10.19	91.5	186.56	5.70		1.5007
PdV-6 2-0.5 um	8.982	21.83	76.0	216.05	6.38	Buntsandstein	1.5003
PdV-6 0.5-0.2 um	9.303	18.33	81.6	184.31	5.27	246 - 251 Ma	1.5007
PdV-6 <0.2 um	7.756	22.28	82.6	197.88	5.59		1.5007
PdV-7 2-0.5 um	6.367	14.55	63.5	138.83	4.85	Buntsandstein	1.5003
PdV-7 0.5-0.2 um	6.868	11.04	48.1	133.31	6.48	246 - 251 Ma	1.5003
PdV-7 <0.2 um	6.622	10.59	83.7	139.98	4.06		1.5003
CT-4 2-0.5 um	5.375	11.82	90.8	235.04	6.73	Keuper	
CT-4 0.5-0.2 um	5.339	16.55	89.5	202.55	5.56	200 - 235 Ma	
CT-4 <0.2 um	6.097	20.02	88.0	175.31	4.87		

https://doi.org/10.1180/clm.2025.10014 Published online by Cambridge University Press

Table4

Data point	SiO_2	Al_2O_3	CaO	MgO	Na_2O	K_2O	Fe_2O_3	MnO	TiO_2	SUM	Identification
PdV-7 / 1 .	40.00	12.74	0.01	3.14	0.18	9.15	23.10	0.15	1.15	89.6	Illite replacing biotite
PdV-7 / 2 .	39.45	12.59	0.05	3.20	0.25	8.92	23.75	0.02	1.00	89.2	Illite replacing biotite
PdV-7 /3	40.27	12.95	0.05	3.82	0.27	9.22	24.45	0.18	0.78	92.0	Illite replacing biotite
PdV-7 /4	50.84	31.88	0.15	2.05	0.10	8.99	1.23	0.00	0.00	95.2	Illite replacing feldspar
PdV-7 /5	50.17	31.86	0.08	2.32	0.05	8.53	1.21	0.00	0.00	94.2	Illite replacing feldspar
PdV-7 /6	50.27	31.27	0.10	2.40	0.05	8.20	1.36	0.00	0.14	93.8	Illite replacing feldspar
PdV-7 /7	57.65	21.62	0.10	3.68	0.16	6.41	2.66	0.04	0.00	92.3	Matrix illite
PdV-7 /9	57.84	25.00	0.17	3.46	0.14	6.75	2.54	0.03	0.00	95.9	Matrix illite
PdV-7 /10	57.65	23.51	0.16	3.33	0.15	6.45	3.00	0.00	0.06	94.3	Matrix illite
PdV-7 /11	61.23	21.05	0.13	2.94	0.07	5.76	2.91	0.03	0.01	94.2	Matrix illite

Data point	PdV-7 /4	PdV-7 /5	PdV-7 /6	PdV-7 /7	PdV-7 /9	PdV-7 /10	PdV-7 /11	PdV-7 /11corr	PdV-7 / 1	PdV-7 / 2	PdV-7 /3
Identification	**Illite replacing feldspar**			**Matrix illite**					**Illite replacing biotite**		
Si	3.32	3.30	3.32	3.81	3.69	3.74	3.93	3.76	3.16	3.13	3.10
Al^{IV}	0.68	0.70	0.68	0.19	0.31	0.26	0.07	0.24	0.84	0.87	0.90
Al^{VI}	1.77	1.78	1.76	1.50	1.57	1.53	1.53	1.53	0.34	0.30	0.27
Fe	0.06	0.06	0.07	0.13	0.12	0.15	0.14	0.16	1.37	1.42	1.42
Mg	0.17	0.16	0.17	0.36	0.31	0.32	0.28	0.31	0.37	0.38	0.44
Layer charge	-0.85	-0.86	-0.84	-0.57	-0.62	-0.58	-0.50	-0.56	-0.95	-0.95	-0.95
Oct. cations	2.00	2.00	2.00	1.99	2.00	2.00	1.95	2.00	2.09	2.10	2.13
Ca	0.01	0.01	0.01	0.01	0.01	0.01	0.01	0.01	0.00	0.00	0.00
Na	0.01	0.01	0.01	0.02	0.02	0.02	0.01	0.01	0.03	0.04	0.04
K	0.75	0.72	0.69	0.54	0.55	0.53	0.47	0.53	0.92	0.90	0.91
Mg	0.03	0.06	0.07	0.00	0.02	0.00	0.00	0.00	0.00	0.00	0.00
NH_4	0.00	0.00	0.00	0.00	0.00	0.00	0.00	0.00	0.00	0.00	0.00
Interlayer ch.	0.85	0.86	0.84	0.57	0.62	0.58	0.50	0.56	0.95	0.95	0.95

https://doi.org/10.1180/clm.2025.10014 Published online by Cambridge University Press